ELSEVIER

Application of roughness-dependent boundary conditions to turbulent oscillatory flows

S. G. Sajjadi and M. N. Waywell
Centre for Computational Fluid Dynamics and Turbulence, University of Salford, Salford, UK

The purpose of this paper is to model wave-induced oscillatory flows traversing rough beds using high-Reynolds number turbulence models based on boundary conditions that are sensitized to the local state of bed roughness (be it hydraulically smooth, transitional, or fully rough). Such boundary conditions replace more traditional approaches (based on a no-slip velocity condition), which are, hitherto, most commonly applied to the majority of oceanographic and estuarine calculations. Both eddy-viscosity and differential second-moment (DSM) closures are implemented and compared with experimental data. It is shown that the linear length scale used in the eddy-viscosity k-ℓ model will lead to serious errors. This paper should, therefore, convey the message to coastal and marine engineers that, eddy-viscosity models, such as the k-ℓ model, that are still employed in the vast majority of coastal engineering simulations and are used to calculate parameterized flow coefficients used in large-scale three-dimensional hydrodynamic codes, such as those for predicting internal tides and sediment transport, should be replaced by advanced turbulence transport models. The other aim of this paper is to show how near-bed predictions of turbulent kinetic energy profiles on rough boundary layers, whose roughness is related to Nikuradse sand grains, can be improved. It is demonstrated that when wall-function boundary conditions (sensitized to the bed roughness) are used, in favour of a more traditional non-slip velocity strategy, a better agreement with experimental data is achieved.

Keywords: turbulence modelling, oscillatory flows, rough boundary layer

Introduction

Wave-induced oscillatory flows (of oscillation period $T \approx 8 - 10$ s) are readily observed in many different oceanographic flow environments. Such flows are driven by wind waves and can occur either in isolation (Davies 1991; Davies and Jones 1991) or more commonly they interact with tidally induced motions ($T \approx 12$ h), see Davies et al. (1988). At high enough Reynolds numbers, turbulence generated at the sea bed increases the bed stress significantly. This leads to increases rates of marine sediment erosion. Therefore, an understanding of turbulent oscillatory boundary layers is important to coastal engineers interested in the prediction of bed erosion and suspended sediment transport in coastal and estuarine environments, where significant wave action is found (see, for example, Aldridge 1990; Bowden and Ferguson 1980; Gordon and Dohne 1973; Hamilton et al. 1980).

A number of experimental studies have made new contributions to our understanding of the turbulent behaviour of oscillatory flow over both smooth and rough boundaries (Akhavan et al. 1991; Hino et al. 1983; Jensen et al. 1989; Jonsson and Carlsen 1976; Sleath 1987, 1988; Sumer et al. 1988). From these studies, it is clear that turbulence is generated in the vicinity of near-bed regions either through shear layer instability or the turbulence-bursting phenomenon (Jensen et al.; Hino et al.; Anwar and Atkins 1980; and Gordon 1975, for tidally induced flows).

Computational predictions of turbulent oscillatory flows traversing rough beds have also been reported. Examples include the simulations of Justesen and Fredsøe (1985), Davies and Jones (1991), Justesen (1988), Hagatun and Eidsvik (1986), and Aldridge (1990). However, all of these investigations employ high-Reynolds number eddy-viscosity models. The assumptions of isotropic eddy-viscosity models are often weak in the vicinity of near-wall anisotropic regions. Clearly, the implementation of isotropic eddy-viscosity models is not sufficient to capture near-wall turbulence energy levels accurately: a fact hitherto ignored by coastal and marine engineers. On such environmental flows only Brørs and Eidsvik (1995) and Sajjadi and Aldridge (1995) have recently applied differential second - moment (DSM) closure schemes and achieved better agreement with experimental data.

Perhaps the most contentious issue associated with rough bed numerical simulations, which is also of special interest here, is the prescription of rough bed boundary conditions at rough beds. Because every rough bed has its own unique characteristics, the only practical approach is to parameterize the roughness parti-

Address reprint requests to Dr. S. G. Sajjadi, Centre for Computational Fluid Dynamics, University of Salford, Salford M5 4WT, UK

Received 29 March 1996; accepted 10 December 1996

Int. J. Heat and Fluid Flow 18:368–375,1997

655 Avenue of the Americas, New York, NY 10010

0142-727X/97/$17.00
PII S0142-727X(97)00021-0

cles through a single roughness length. This idea was first investigated by Nikuradse (1933), who scaled all rough bed distributions onto a single roughness length scale k_s: the Nikuradse roughness equivalence. Nikuradse also proposed suitable boundary conditions for rough beds based on the experimental observations of a variety of steady, fully turbulent, and fully rough boundary layers. In the same paper, Nikuradse concluded that a no-slip velocity condition could be applied at a roughness length $Y_0 = k_s/30$ above the theoretical bed level (approximately $2/3d$ above the base of the sane grains; d being the sand grain diameter). The empirical length Y_0 is assumed to be much larger than the near-bed semiviscous region where high-Reynolds number turbulence closures are invalid. However, apart from the fully rough state, Schlichting (1968) notes that there are two other local states of bed roughness classified as follows:

(1) hydraulically smooth regime ($k_s^+ \leq 5$);

(2) transitional regime ($5 < k_s^+ \leq 70$); and

(3) fully rough turbulent regime ($k_s^+ > 70$).

Here $k_s^+ = U_\tau k_s/\nu$ defines the dimensionless roughness height and $U_\tau = \sqrt{\tau_w/\rho}$ is the wall friction velocity. Experimental data recorded in turbulent oscillatory flow regimes indicate that the rough bed does not remain fully rough across the entire flow cycle, particularly around flow reversal, where the bed acts as if hydraulically smooth (Jensen et al. 1989). This implies that the traditional approach to rough bed boundary conditions based on the experimental findings of Nikuradse (1933) may not be sufficient to model turbulent oscillatory flows accurately. To investigate this point further, the present contribution employs boundary conditions based on the wall-function approach of Launder and Spalding (1974), which are sensitized to the local state of bed roughness through the dimensionless parameter k_s^+.

Because experimental data in coastal flows are expensive (and often impossible) to collect, there is a pressing need in the coastal engineering community to estimate sediment transport (usually pollutants) over large-scale coastal regions extending over hundreds of kilometres. Aldridge and Davies (1993) applied a three-dimensional (3-D) hydrodynamic model to simulate the Eastern Irish Sea. High-resolution simulations naturally involve a serious computational penalty in the form of a spiralling central processing unit (CPU) budget. In an attempt to reduce costs, most large-scale tidal models are based on the one-equation k–ℓ eddy-viscosity model. Furthermore, slip boundary conditions are usually applied at a distance 100-cm above the sea bed. This also reduces costs, because the high mean rates-of-strain in the near-bed region need not be resolved. For example, the bed stress is related to the slip velocity U_{100} by the relationship $\tau_w = \rho C_{100} U_{100}^2$, where C_{100} is a drag coefficient evaluated 1 metre above the sea bed. This drag coefficient is a function of bed roughness and is affected by small-scale features. These small-scales cannot be resolved by large-scale coastal models. Instead, the effects of these small-scale features can only be parameterized, and appropriate values of C_{100} can, in principle, be determined through detailed modelling of small-scale flow problems (Bowden and Ferguson 1980; Sajjadi and Aldridge 1995). However, to date most coastal engineers adopt an eddy-viscosity model that is often based on linear length-scale distribution. Indeed, it is well known that the validity of the assumption of a linear length-scale distribution to the edge of the boundary layer made with the one-equation k–ℓ model is questionable. One aim of this paper is to demonstrate that such a choice in turbulence model for parameterizing bottom boundary conditions, used in large-scale (3-D) hydrodynamic codes, leads to serious errors.

A better choice of turbulence model would be a two-equation k–ε scheme. Although these models are not particularly inferior to second-moment closure schemes, for the type of flows considered here, it does have a drawback, because the turbulent stresses have to be calculated from an algebraic relationship rather than from the solution of their transport equation. In view of the present day computational power, we might as well adopt a second-moment closure model and, thus, obtain a more accurate result for turbulent stresses.

Finally, we argue in the Results section that the poor prediction obtained at certain phases can be attributed to the fact that in the experiment, the flow is laminarizing or is essentially laminar. This, of course, cast doubts on the whole approach of using high-Reynolds number versions of the models. The alternative is the use of their low-Reynolds number counterparts. However, at present, no such models exist that can be applied to rough boundaries, where the roughness is function of Nikuradse roughness element.

Mathematical description

If the wave amplitude $a = U_\infty/\omega$, where U_∞ is the peak free-stream velocity outside the boundary layer and ω the frequency, is small compared to the wavelength λ, it is permissible to neglect the advective acceleration terms in comparison with the temporal acceleration term in the momentum equation. This approximation is consistent with the assumption of a linear water wave (for which the surface slope a/λ is vanishingly small) driving the flow. The streamwise velocity U then satisfies:

$$\rho \frac{\partial U}{\partial t} = -\frac{\mathrm{d}P}{\mathrm{d}x} + \frac{\partial}{\partial y}\left\{\mu \frac{\partial U}{\partial y} - \rho\overline{uv}\right\} \tag{1}$$

Here, the mean velocity at the edge of the boundary layer is assumed to be given by $U = U_\infty \sin \omega t$, where $\omega = 2\pi/T$; T being the period of oscillation. Assuming the turbulent Stokes layer is small compared to the vertical length-scale (i.e., the channel half-width h) the value of the pressure gradient inside the boundary layer is assumed to equal the free-stream value. In the free stream, vanishing rates of strain replace the pressure gradient by the temporal velocity acceleration $(\partial U/\partial t)_{y=h}$ so that:

$$\frac{\mathrm{d}P}{\mathrm{d}x} = -\rho U_\infty \omega \cos \omega t \tag{2}$$

To solve Equation 1, we must determine the turbulent shear stress $\overline{uv}$ using a closure scheme. In this paper, we adopt three closure strategies. The first two are the well-known eddy-viscosity, one-equation k–ℓ and two-equation k–ε models in which the Reynolds shear stress is related to the mean rates of strain by (Boussinesq 1877)

$$-\rho\overline{uv} = \rho \nu_t \frac{\partial U}{\partial y} \tag{3}$$

Here ν_t is the eddy-viscosity given by

$$\nu_t = c_\mu \frac{k^2}{\varepsilon} \tag{4}$$

where $c_\mu = 0.09$, k denotes the turbulent kinetic energy, and ε represents the turbulent dissipation rate. The equations governing the transport of k and ε (within the same order of approximation as that of mean momentum equation) are, respectively

$$\frac{\partial k}{\partial t} = \frac{\partial}{\partial y}\left\{\frac{\nu_t}{\sigma_t}\frac{\partial k}{\partial y}\right\} - \overline{uv}\frac{\partial U}{\partial y} - \varepsilon \tag{5}$$

for k–ℓ model:

$$\varepsilon = \frac{c_\mu^{3/4} k^{3/2}}{\kappa y} \tag{6}$$

for k–ε model:

$$\frac{\partial \varepsilon}{\partial t} = \frac{\partial}{\partial y}\left\{\frac{\nu_t}{\sigma_\varepsilon}\frac{\partial \varepsilon}{\partial y}\right\} - \left(c_{\varepsilon 1}\overline{uv}\frac{\partial U}{\partial y} + c_{\varepsilon 2}\varepsilon\right)\frac{\varepsilon}{k} \tag{7}$$

The model constants are given in Table 1.

The third applied closure is the differential second-moment model (herein referred to as DSM). In contrast to the eddy-viscosity models, the turbulent shear stress $\overline{uv}$ is determined from its transport equation. Of course, in the second-moment methodology, the shear stress cannot be found independent of the Reynolds-stress components. Each is described by the following equation, written in Cartesian tensor form, as

$$\underbrace{\frac{D\overline{u_i u_j}}{Dt}}_{C_{ij}} + \underbrace{-\left\{\overline{u_i u_k}\frac{\partial U_j}{\partial x_k} + \overline{u_j u_k}\frac{\partial U_i}{\partial x_k}\right\}}_{P_{ij}}$$

$$\underbrace{-\frac{\partial}{\partial x_k}\left\{\underbrace{\overline{u_i u_j u_k}}_{d_{ij}^t} + \underbrace{\overline{\frac{p}{\rho}(\delta_{jk}u_i + \delta_{ik}u_j)}}_{d_{ij}^p} - \underbrace{\nu\frac{\partial \overline{u_i u_j}}{\partial x_k}}_{d_{ij}^v}\right\}}_{d_{ij}}$$

$$\underbrace{+\overline{\frac{p}{\rho}\left\{\frac{\partial u_i}{\partial x_j} + \frac{\partial u_j}{\partial x_i}\right\}}}_{\phi_{ij}} \underbrace{- 2\nu\overline{\frac{\partial u_i}{\partial x_k}\frac{\partial u_j}{\partial x_k}}}_{\varepsilon_{ij}}$$

In the above equation, the terms have been grouped, following a well-established practice, so as best to allow a physical interpretation of the processes. A shorthand symbol is given for each process, which we use to simplify latter equations. The first two processes represent, respectively, the convection term C_{ij} and rates of creation of $\overline{u_i u_j}$ by the effects of mean strain P_{ij}, which are both exact and require no modelling. However, the diffusion term d_{ij}, pressure re-distribution term ϕ_{ij}, and the destruction rate of $\overline{u_i u_j}$ by viscous action ε_{ij} cannot be accounted for without further approximation. The DSM closure presented here is based on the original proposal of Gibson and Launder (1978) with the exception that the Daly and Harlow (1970) gradient diffusion hypothesis for the diffusion term d_{ij} is replaced by the isotropic model of Shir (1973)

$$d_{ij} = \frac{\partial}{\partial x_k}\left\{\frac{c_\mu}{\sigma_t}\frac{k^2}{\varepsilon}\frac{\partial \overline{u_i u_j}}{\partial x_k}\right\} \tag{8}$$

This term collectively models diffusive transport attributable to fluctuating turbulent velocities, d_{ij}^t, and fluctuating pressures, d_{ij}^p. Molecular diffusion

$$d_{ij}^v = \frac{\partial}{\partial x_k}\left(\nu\frac{\partial \overline{u_i u_j}}{\partial x_k}\right)$$

is negligible in high-Reynolds number turbulence.

The correlation between fluctuating pressure and fluctuating strain ϕ_{ij}, is a very important one. We note that its trace is zero, because by continuity the divergence of the velocity fluctuation vanishes. This term, therefore, makes no contribution to the overall level of turbulence energy but serves to redistribute energy among the normal stress components (those for which $i = j$). The best physical interpretation of the process is understood by breaking ϕ_{ij} down into four distinct mechanisms:

$$\phi_{ij} = \underbrace{-c_1\varepsilon a_{ij}}_{\phi_{ij1}} \underbrace{-c_2(P_{ij} - 2/3\delta_{ij}P_{kk})}_{\phi_{ij2}}$$

$$\underbrace{+ c_1^w\frac{\varepsilon}{w}(\overline{u_k u_m}n_k n_m\delta_{ij} - 3/2\overline{u_k u_i}n_k n_j - 3/2\overline{u_k u_j}n_k n_i)f}_{\phi_{ij1}^w}$$

$$\underbrace{+ c_2^w(\phi_{km2}n_k n_m\delta_{ij} - 3/2\phi_{ik2}n_k n_j - 3/2\phi_{jk2}n_k n_i)f}_{\phi_{ij2}^w} \tag{9}$$

Terms ϕ_{ij1} and ϕ_{ij2} are frequently referred to as the "return-to-isotropy" and "rapid" terms of the pressure-strain, respectively. The return-to-isotropy terms tends to steer the turbulence field towards an isotropic state, while the rapid term tends to make the production tensor P_{ij} more isotropic (*Isotropization of Production* or DSM-IP model).

Pressure fluctuations reflecting from rigid boundaries are represented by terms ϕ_{ij1}^w and ϕ_{ij2}^w. This "echoing" is responsible for a transfer of wall-normal stresses to wall-parallel stresses and imprints a measure of near-wall stress anisotropy. The controlling factor of the process is the function $f = k^{3/2}/\varepsilon y$, which is the ratio of the local length-scale to the wall-normal distance y. Terms n_i denote the unit vector normal to the wall, where for a flat plate, $n_i = (0, 1, 0)$.

For high-Reynolds number models, the dissipation rate of turbulence energy by viscous action is assumed to be isotropic. Thus, we assume

$$\varepsilon_{ij} = \tfrac{2}{3}\delta_{ij}\varepsilon \tag{10}$$

where ε is obtained from its own transport equation

$$\frac{\partial \varepsilon}{\partial t} = \frac{\partial}{\partial y}\left\{c_\varepsilon\frac{k}{\varepsilon}\overline{v^2}\frac{\partial \varepsilon}{\partial y}\right\} + \frac{\varepsilon}{2k}c_{\varepsilon 1}P_{kk} - c_{\varepsilon 2}\frac{\varepsilon^2}{k} \tag{11}$$

which was originally proposed by Launder et al. (1975).

In the present scheme, the turbulent kinetic energy is calculated from the following transport equation

$$\frac{\partial k}{\partial t} = \frac{\partial}{\partial y}\left\{\frac{c_\mu}{\sigma_t}\frac{k^2}{\varepsilon}\frac{\partial k}{\partial y}\right\} - \overline{uv}\frac{\partial U}{\partial y} - \varepsilon \tag{12}$$

The normal stress $\overline{w^2}$ is then obtained from $\overline{w^2} = 2k - (\overline{u^2} + \overline{v^2})$. The DSM-IP model constants are given in Table 2.

Table 1 Model constants for the eddy-viscosity models

σ_t	σ_ε	$c_{\varepsilon 1}$	$c_{\varepsilon 2}$
1.0	1.3	1.45	1.92

Table 2 Model constants for the DSM-IP model

c_μ	σ_t	c_ε	$c_{\varepsilon 1}$	$c_{\varepsilon 2}$	c_1	c_2	c_1^w	c_2^w
0.065	0.81	0.15	1.45	1.92	1.8	0.6	0.5	0.3

Boundary conditions

The form of models that have been presented above are valid only for fully turbulent flows. Close to solid walls, however, there are inevitably regions where the local Reynolds number of turbulence $\mathrm{Re}(\equiv k^{1/2}l/\nu$, where $l \equiv k^{3/2}/\varepsilon)$ is so small that viscous effects predominate over turbulent ones. In these regions, the present closure models adopted are no longer valid, and the semiviscous near-wall regions must be bridged by a different model. For this we use the well-known wall-function approach (Launder and Spalding 1974).

The present wall-function approach relies on the assumption that the near-wall region lying between the wall and the near-wall computational node is represented by two layers: a wall-adjacent fully viscous sublayer and, adjacent to it, a fully turbulent layer, where the velocity profile has the form

$$U = \frac{U_\tau}{\kappa} \ln\left\{\frac{y}{y_0}\right\} \tag{13}$$

and $\kappa = 0.4$ is the von Kármán constant. In Equation 13, y is the vertical distance measured from the base of the sand gains, and the parameter y_0 is determined by the state of the roughness at the boundary (hydraulically smooth, transitional, or fully rough). Choosing the velocity scale in the log-law region to be proportional to $k^{1/2}$, the form of y_0 is given by

$$y_0 = \frac{\mu}{E\rho c_\mu^{1/4} k^{1/2}} \tag{14}$$

where E is a roughness coefficient evaluated as in Krishnappen (1984) by the following expression

$$E = \frac{\exp(\kappa B_s)}{k_s^+} \tag{15}$$

Sajjadi and Aldrige (1995) have adopted the following formula for B_s:

$$B_s(k_s^+) = \begin{cases} \left(5.5 + \dfrac{1}{\kappa} 2.5 \ln k_s^+\right) e^{-0.062(\ln k_s^+)^3} & \\ \qquad +8.5(1 - e^{-0.062(\ln k_s^+)^3}) & \text{if } k_s^+ > 1 \\ 5.5 + \dfrac{1}{\kappa} 2.5 \ln k_s^+ & \text{if } k_s^+ \le 1 \end{cases} \tag{16}$$

The above formula yields the asymptotic value for y_0 in the smooth and rough regions according to whether $k_s^+ \to 0$ or $k_s^+ \to \infty$, respectively. The form given above represents an excellent fit to Nikuradse's (1933) measurements as shown in Figure 1. The boundary condition for $\overline{uv}$ at the lowest computational node is

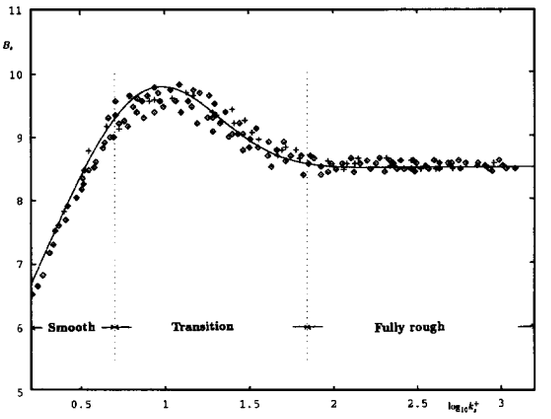

Figure 1 Relationship between B_s and k_s^+, ◇ and + experimental data from Nikuradse (1933);—Equation 16

determined from the approximation of a constant shear stress near the wall. We, therefore, set

$$(\overline{uw})_N = \frac{\tau_w}{\rho} \tag{17}$$

Values of normal Reynolds stresses and turbulent kinetic energy in the wall-neighbouring control volume are determined from the solution of their corresponding transport equations, incorporating the volume-integrated production terms. More detail can be found in the recent paper by Sajjadi and Aldridge (1995).

The dissipation rate within the wall-adjacent cell is calculated assuming a linear near-wall variation of turbulent length scale as

$$\varepsilon_N = \frac{c_\mu^{3/4} k_N^{3/2}}{\kappa y_N} \tag{18}$$

Finally, the upper boundary conditions for turbulent variables are:

$$\frac{\partial k}{\partial y} = \frac{\partial \varepsilon}{\partial y} = \frac{\partial \overline{u^2}}{\partial y} = \frac{\partial \overline{v^2}}{\partial y} = \overline{uv} = 0 \tag{19}$$

The computational procedure for the governing equations is based on the fully conservative, structured finite-volume framework, within which the volumes are collocated so that all flow variables are stored at one and the same set of nodes. Numerical stability is achieved through the implementation of apparent viscosities, as has been demonstrated by Sajjadi and Aldridge (1995).

Results

The closure models were calibrated and compared with the experimental data of Jensen et al. (1989) and Sumer et al. (1988). All the results presented in this paper are comparisons in the half-range $\omega t = 0°$–$180°$. This half-range is again subdivided into two flow stages—(1) the first acceleration phase $\omega t = 0°$–$75°$, and (2) the first deceleration phase $\omega t = 90°$–$165°$. The important flow parameters are defined in Table 3.

Table 3 Flow parameters for the experimental data

Source	U_∞ (m/s)	a (m)	k_s (m)	a/k_s	ω (rad)	T (s)	Re
Jensen et al. (1989)	2.1	3.1	0.84×10^{-3}	3690	0.646	9.72	5.7×10^6
Sumer et al. (1988)	2.1	2.71	3.75×10^{-3}	720	0.774	8.12	5.0×10^6

The experimental setup in both cases was very similar, with data measured in a U-shaped oscillatory flow channel. The working section was 10-m long with height $H = 0.3$ m where $H = 2h$ ($h \equiv$ channel half-width). In the Jensen et al. (1989) test case, roughness was introduced onto a smooth perspex bed by gluing down sheets of sandpaper with particle density 80 grains/cm^2. Oscillating waves were generated by an electronically controlled pneumatic system. Experimental data were collected along the channel half-width $0 \le y \le h$. The main difference between the experimental trials is the increased size of the sand grains in the Sumer et al. (1988) data. From the experimental data, we note that compared to the Jensen et al. study, near-bed turbulent kinetic energy predictions are approximately 40% higher for the Sumer et al. experiment. This is because of the increased particle size of the bed, which induces more drag on the flow and, therefore, raises near-bed levels of turbulence.

Comparison with Jensen et al. (1989) experimental data

Figures 2(a, b) demonstrate predictions of normalised mean velocity profiles U/U_∞ by the DSM-IP and k-$\mathscr{l}$ models compared with experimental data across the half-cycle. The abscissa represents the normalised distance, y/a, which is plotted on a logarithmic scale. During the first acceleration state ($0° \le \omega t \le 75°$), it is clear that both of the turbulence closures capture the development of the logarithmic region, which begins at $\omega t = 0°$ and is completed at $\omega t = 30°$. Note that, between $0° \le \omega t \le 30°$, the flow is not fully turbulent. Throughout the accelerating stage, the DSM-IP module compares more favourably with experimental data than the k-$\mathscr{l}$ model. We also note that both of the turbulence models underpredict the "wake-like" region (situated below the free-stream region at $y/a \approx 0.015$) towards the end of the accelerating stage. The eddy-viscosity model is in very serious disagreement with experimental data, but the DSM-IP model, at least, captures the qualitative trend of the experimental wake component.

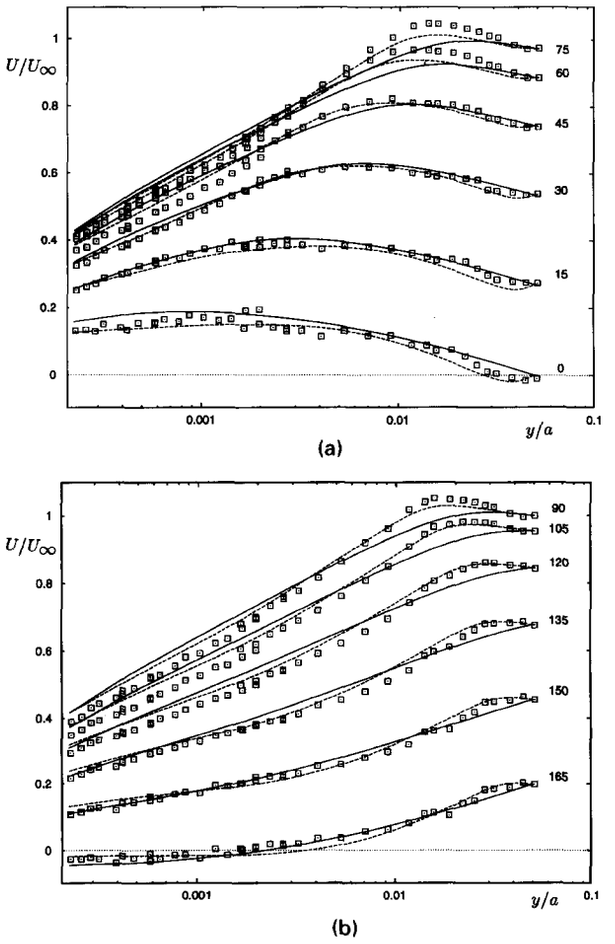

Figure 2 Normalised mean velocity predictions across the half-cycle: (i) first acceleration stage; (ii) first deceleration stage: —k-$\mathscr{l}$ model; - - - DSM-IP model; □ experimental data from Jensen et al. (1989)

After pressure gradient reversal (at $\omega t = 90°$), the flow begins to decelerate, as shown in Figure 2(b). Throughout the first acceleration stage, we note that near-bed experimental data are spread out more during the decelerating stage than the accelerating stage, although both the DSM-IP and k-$\mathscr{l}$ models continue to be in good accord with experimental data. After $\omega t > 135°$, the logarithmic region and wake-like component begin to decay. Although both of the turbulence closures capture the decay of the logarithmic region satisfactorily, only the DSM-IP resolves the decay of the wake-like region. In contrast, the k-$\mathscr{l}$ model smears out experimental data in the vicinity of the wake-like component.

Turbulent kinetic energy predictions by the k-$\mathscr{l}$ and DSM-IP models compared with experimental data across the half-cycle are presented in Figures 3(a, b). The experimental form of k is that taken from Mendoza and Shen (1990):

$$k = \tfrac{1}{2}(\overline{u^2} + 2\overline{v^2}) \tag{20}$$

Turbulent energy begins to build up in the near-bed region during the early phases of the accelerating stage. This feature is characterised by the rapid growth of a sharp near-bed peak. The production of energy during the acceleration stage is associated with shear-layer instability, but the growth of turbulence energy is generally restricted to the near-bed region. Away from the bed, energy levels remain low at residual levels. The DSM-IP and k-$\mathscr{l}$ models capture the growth of near-bed energy during the early phases of the accelerating stage, but after $\omega t > 45°$, both models overpredict experimental data (the k-$\mathscr{l}$ model very seriously). Away from the wall, the k-$\mathscr{l}$ model also overpredicts experimental data throughout the half-cycle; whereas, the DSM-IP model underpredicts it. However, we note that the DSM-IP is in very good agreement with experimental data throughout the cross section of the channel during the final stages of the accelerating stage.

With the onset of pressure-gradient reversal, turbulence energy grows violently and explosively in the vicinity of the bed during the early phases of the first deceleration stage. This is a consequence of the turbulence-bursting phenomenon. The bursting ejects turbulence energy upwards towards the free-stream region. We note that the DSM-IP model is in good agreement with experimental data along the depth of the channel during the early phases of the deceleration stage. In contrast, the k-$\mathscr{l}$ model overpredicts experimental data both near to and far from the bed. However after $\omega t > 135°$, production of turbulence energy in the near-bed ceases, and both models underpredict experimental data in the vicinity of the bed, although the DSM-IP model clearly improves on the k-$\mathscr{l}$ predictions. Above $y/a > 0.03$, the DSM-IP model seriously underpredicts experimental data. Conversely the k-$\mathscr{l}$ model overpredicts experimental data as the free-stream region is approached.

Disagreement with the experiment in the latter phases of the deceleration stage is attributed to two reasons. Firstly high-Reynolds number models cannot resolve the turbulence-bursting phenomenon accurately. It is interesting to note that Hanjalić (1994) and Hanjalić et al. (1993) applied a low-Reynolds number DSM cubic model to an oscillatory flow traversing a smooth bed

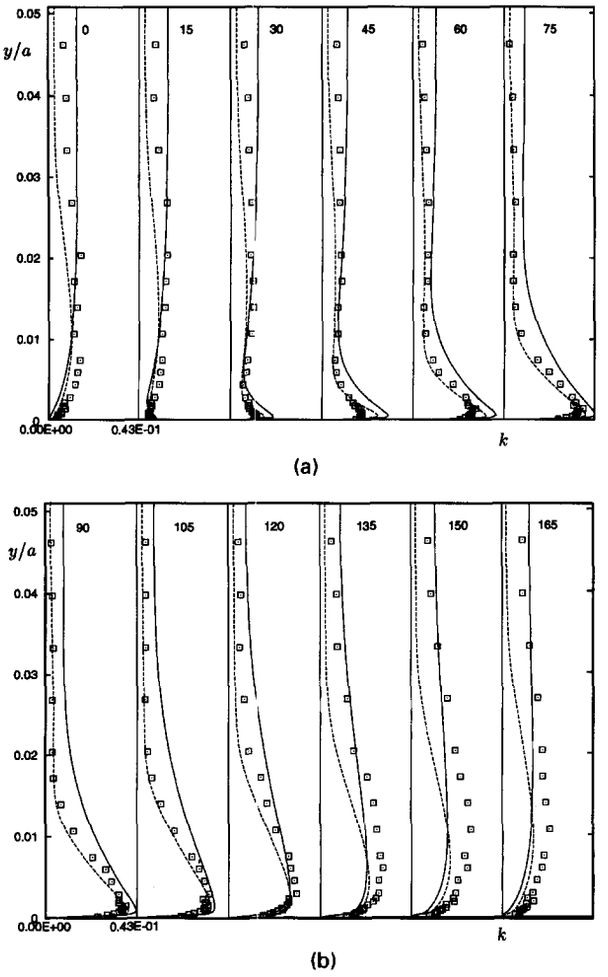

Figure 3 Turbulent kinetic energy predictions across the half-cycle: (i) first acceleration stage; (ii) first deceleration stage: —k-ℓ model; - - - DSM-IP model; □ experimental data form Jensen et al. (1989)

and successfully resolved the bursting phenomenon in the bed stress profiles. Secondly, as the decelerating stage progresses, the pressure gradient becomes increasingly adverse, stopping the production of turbulence energy in the near-bed region and, thus, beginning the relaminarization process. Because the high-Reynolds number models presented here are based on the assumptions of high-Reynolds number turbulence, it is unlikely that such models will be able to predict experimental data in intrinsically laminar flow phases. Also noteworthy is the fact that the best DSM-IP comparisons with the experiment occur during the fully developed turbulence regime $60° \leq \omega t \leq 120°$, where the high-Reynolds number modelling assumptions are strong.

Finally, as previously explained, traditional boundary conditions are independent of the state of bed roughness and were originally developed for fully rough boundary layers. This amounts to a nonphysical interpretation of the exact influence of the roughness elements on the oscillatory flow. This is illustrated in Figure 4, where we compare the predicted variation of k_s^+ by the k-ℓ and DSM-IP models with the experimental data of Jensen et al. (1989). The sharp minimum (around 165°) represents flow reversal. At this phase, the flow is intrinsically laminar, and the wall acts hydraulically smooth. Clearly, the sand grains cannot be considered to be fully rough. The rough wall acts fully rough in the phase interval $40° < \omega t < 100°$, that is to say, in only one-third

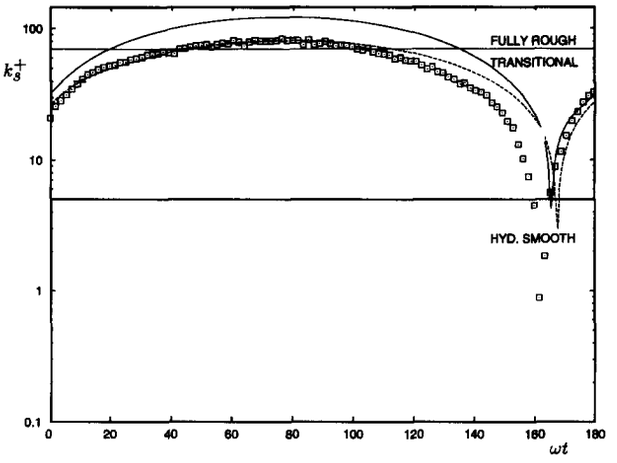

Figure 4 Variation of k_s^+ across the half-cycle: —k-ℓ model; - - - DSM-IP model; □ experimental data from Jensen et al. (1989)

of the half-cycle. This reinforces the need for turbulence closures to account for the local state of bed roughness in turbulent oscillatory flow calculations.

Comparison with Sumer et al. (1988) experimental data

In a second series of calculations, we compare DSM-IP and k-ℓ predictions with the experimental data of Sumer et al. (1988). From Table 3, we note that, compared with the Jensen et al. (1989) experimental data, the Nikuradse roughness equivalence of the Sumer data is approximately four and one half-times larger. We will, therefore, expect higher levels of turbulence energy in the vicinity of the roughness particles.

Normalised mean velocity profiles plotted against experimental data are represented across the phase interval $90° \leq \omega t \leq 180°$ in Figure 5 (for brevity, we have only shown the decelerating stage). Again, the half-range is subdivided into an accelerating stage $15° \leq \omega t \leq 75°$ and a decelerating stage $90° \leq \omega t \leq 180°$. We note that the experimental predictions reproduce the salient features observed in the Jensen et al. (1989) experimental data during the accelerating stage; namely, the development of the logarithmic region and wake-like component. Once more we note that both models are in good agreement with experimental

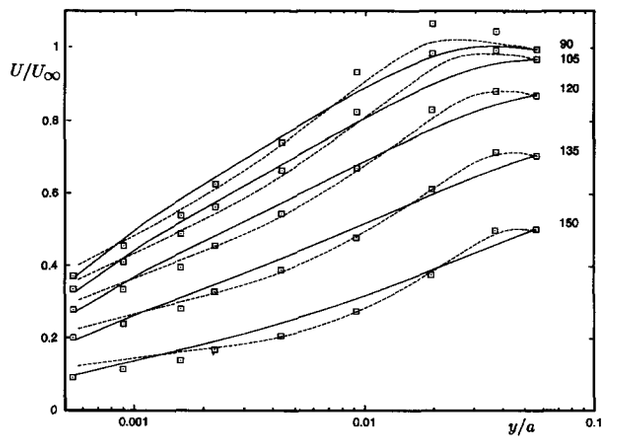

Figure 5 Normalised mean velocity predictions across the half-cycle, first deceleration stage: —k-ℓ model; - - - DSM-IP model; □ experimental data from Sumer et al. (1988)

data in the logarithmic region. However, both models underpredict the wake-like region during the latter phases of the acceleration state (although the DSM-IP model is still in better agreement with experiment than the one-equation model). Also noteworthy are the reduced values of U/U_∞ in the vicinity of the bed compared with the Jensen data. This feature is a consequence of the larger roughness particles used in the Sumer et al. (1988) data, which have a greater tendency to retard near-bed fluid particles.

For $\omega t > 90°$, the fluid decelerates, and both the logarithmic region and the wake-like component slowly decay, but, again, as can be seen from Figure 5, the k-ℓ model smears out the experimental data throughout decelerating stage. We also note that like the Jensen et al. (1989) data, near-bed predictions of U/U_∞ are more spread out during the decelerating stage compared with the accelerating stage, a feature captured satisfactorily by both models. In general, though, the DSM-IP model is in better agreement with experimental data than the k-ℓ model.

Figure 6 compares predicted values of turbulent kinetic energy with experimental data, where this time we have followed Justesen (1988) and set

$$k = \tfrac{3}{4}(\overline{u^2} + \overline{v^2}) \tag{21}$$

implying that $\overline{w^2} = 1/2(\overline{u^2} + \overline{v^2})$. Across the acceleration stage, near-bed turbulence energy levels begin to build-up vary rapidly through the action of shear layer instability. We note that across the accelerating stage, the k-ℓ model overpredicts experimental data along the entire depth of the water column. During the early phases of the acceleration stage, the DSM-IP model also overpredicts experimental data, but this is significantly reduced compared to the k-ℓ model. Despite this, the DSM-IP model compares favourably with experimental data along the cross section of the channel throughout the accelerating stage. This trend continues through the early stages of the decelerating stage (not shown here), where the k-ℓ model continues to overpredict experimental data through the depth of the channel. High levels of near-bed turbulence are once more sustained through the turbulence-bursting phenomenon. For $\omega t > 150°$, both models underpredict experiment in the vicinity of the bed, and the flow begins to relaminarize because of an increasingly adverse pressure-gradient. It is during the latter phases of the deceleration stage that the underlying assumptions of high-Reynolds number models are weak.

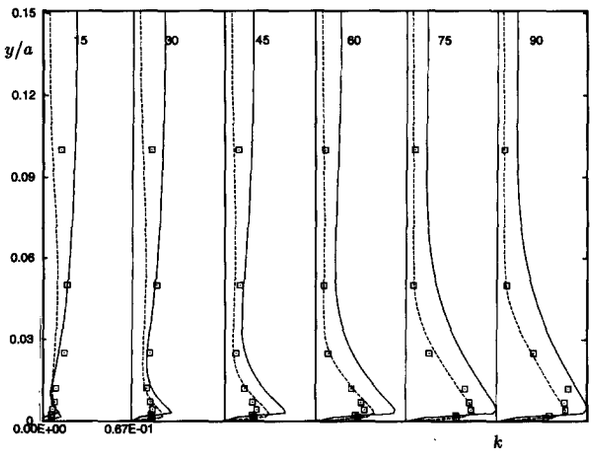

Figure 6 Turbulent kinetic energy predictions across the half-cycle, first acceleration stage: —k-ℓ model; - - - DSM-IP model; □ experimental data from Sumer et al. (1988)

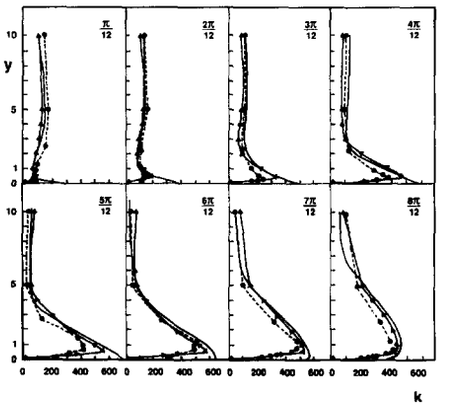

Figure 7 Turbulent kinetic energy predictions across the half-cycle: —Justesen (1998) k-ε model; × present k-ε

In a final calculation, we compare the k-ε simulation of Justesen (1988), who implemented traditional boundary conditions (based on a no-slip boundary condition and local-equilibrium at a roughness length Y_0) with a k-ε simulation, which employs the roughness dependent boundary conditions described earlier (Figure 7). From the figure, we note that the present k-ε model reduces near-bed predictions of k during the initial phases of the accelerating stage compared with Justesen. Away from the bed, both sets of numerical data predict similar levels of k, which rapidly diminish as the free-stream region is approached. Both of these trends continue throughout the fully developed turbulence regime $60° \leq \omega t \leq 120°$. Also noteworthy is the fact that the present k-ε model predicts the local near-bed maxima of k at the correct height above the bed. In the range $0° \leq \omega t \leq 90°$, the Justesen profiles indicate the local maxima to be at the wall itself. After pressure-gradient reversal, the present k-ε model continues to improve on the Justesen predictions along the entire length of the channel. However, for $\omega t > 150°$ (not shown here), the DSM-IP model begins to give values below both the experimental and Justesen profiles. In addition, both computed profiles of k underpredict experimental data away from the wall. It is believed that the poor numerical predictions in this phase interval can be attributed to the fact that the flow regime is essentially laminar there, and therefore, the high-Reynolds number modelling assumptions become inaccurate.

Concluding remarks

In this paper, we have examined wave-induced oscillatory flows traversing rough beds and attempted to model such flows using high-Reynolds number models including two eddy-viscosity modules (k-ℓ and k-ε models) and a differential second-moment closure (DSM-IP). Numerical predictions have been compared to the experimental data of Jensen et al. (1989) and Sumer et al. (1988). It was shown that in order to capture near-bed experimental data satisfactorily, the DSM-IP model must be employed. However, eddy-viscosity models (particularly the k-ℓ model) continue to be the most widespread turbulence closures applied in oceanographic and estuarine simulations (see, for example, Davies et al. 1988; Dabies 1991; Davies and Jones 1991). Furthermore, in large-scale, 3-D hydrodynamic models (Aldridge and Davies 1993), the near-bed region is bridged by parameterizing the bed stress in terms of the mean velocity and a drag coefficient at exactly one metre above the bed. This procedure is optimized by examining the near-bed region of small-scale flows similar to those presented here. Therefore, it may tentatively be argued that the DSM-IP model will deliver a more

accurate parameterization that has hitherto been estimated with eddy-viscosity models.

Two k–ε models were also compared with the experimental data of turbulent kinetic energy of Sumer et al. (1988). The first was based on a wall-function approach, which was sensitized to the local state of bed roughness. The second was taken from the simulations of Justesen (1988), who applied a traditional no-slip velocity boundary condition at a distance Y_0 above the theoretical level of the roughness elements. Over the vast majority of the half-cycle, the present k–ε results were in better agreement with the experimental, particularly in the near-bed region. However, in the later phases of the decelerating stage, both sets of predictions seriously underpredicted experimental data. This feature was also observed in the earlier k–ℓ and DSM-IP predictions and was attributed to two factors. Firstly, during the late phases of the deceleration, the flow is intrinsically laminar. Because all of the turbulence models presented in this paper are based on the assumptions of high-Reynolds number turbulence, it is unlikely that they will be able to resolve such regions accurately. Secondly, the high-Reynolds number models are not able to capture the turbulence-bursting phenomenon that occurs shortly after pressure-gradient reversal. This feature is responsible for the hysteresis effects observed in the turbulent kinetic energy profiles (Anwar and Atkins 1980; Gordon 1975; Waynell and Sajjadi 1996).

To conclude, we believe that we have demonstrated, particularly to coastal and marine engineers, that to obtain better agreement between computation and experiment in the near-wall turbulence energy levels in turbulence oscillatory flows, induced by water waves, we should employ higher-order turbulence models, such as the DSM closure used here, together with a wall boundary condition sensitized to the local state of bed roughness. Furthermore, the use of a linear length-scale that is commonly used in the eddy-viscosity k–ℓ model will lead to serious errors, which in turn affects the parameterization of drag and stresses for use as boundary conditions in large-scale 3-D hydrodynamic codes.

References

Akhavan, R. Kamm, R. D. and Shapiro, A. H. 1991. An investigation of transition to turbulence in bounded oscillatory Stokes flows Part 1. Experiments. *J. Fluid Mech.*, **225**, 395

Aldridge, J. N. and Davies, A. M. 1993. A high-resolution three-dimensional hydrodynamic tidal model of the eastern Irish Sea. *J. Phys. Oceanogr.*, **23**, 207

Aldridge, J. N. 1990. A continuum mixture theory approach to sediment transport with application to turbulent oscillatory boundary layers. Ph.D. thesis, University of Plymouth, Plymouth, UK

Anwar, H. O. and Atkins, R. 1980. Turbulence measurements in simulated tidal flow. *J. Hydraul. Div.*, **8**, 1273

Bouissinesq, J. 1877. Théories de l'écoulement tourbillant. *Mém Présentés par divers Savants Acad. Sci. Inst. Fr.*, **23**.

Bowden, K. F. and Ferguson, S. R. 1980. A numerical model of the combined wave and current bottom boundary layer. In *Marine turbulence* (*Proc. 11th Liege colloq. on ocean hydrodynamics*, J. C. J. Nihoul ed.), Elsevier, Amsterdam

Bradshaw, P. Ferriss, D. H. and Atwell, P. 1967. Calculation of boundary-layer development using the turbulent energy equation. *J. Fluid Mech.*, **28** 593

Brørs, B. and Eidsik, K. J. 1995. Oscillatory boundary layer flows modelled with dynamic Reynolds stress turbulence closure. *Continental Shelf Res.*, **14**, 1455

Daly, B. J. and Harlow, F. H. 1970. Transport equations in turbulence. *Phys. Fluids*, **13**, 2634

Davies, A. G. Soulsby, R. L. and King, H. L. 1988. A numerical model of the combined wave and current bottom boundary layer. *J. Geophys. Res.*, **93**, 491

Davies, A. M. 1991. On using turbulence energy models to develop spectral viscosity models. *Continental Shelf Res.*, **11**, 1313

Davies, A. M. and Jones, J. E. 1991. On the numerical solution of the turbulence energy equations for wave and tidal flows. *Int. J. Numer. Meth. Fluids*, **12**, 17

Gibson, M. M. and Launder, B. E. 1978. Ground effects of pressure fluctuations in the atmospheric boundary layer. *J. Fluid Mech.*, **86**, 491

Gordon, C. M. 1975. Sediment entrainment and suspension in a turbulent tidal flow. *Marine Geol.*, **18**, M57

Gordon, C. M. and Dohne, C. F. 1973. Some observations of turbulent flow in a tidal estuary. *J. Geograph. Res.*, **78**, 1971

Hagatun, K. and Eidsvik, K. J. 1986. Oscillating turbulent boundary layers with suspended sediment. *J. Geophys. Res.*, **91**, 13045

Hanjalić, K. 1994. Advanced turbulence closure models: A view of current status and future prospects. *Int. J. Heat Fluid Flow*, **15**, 178

Hanjalicá, K. Jakirlić, S. and Hadzić, I. 1993. Computation of oscillating turbulent flows at transitional Re-numbers. *Proc. 9th Symposium of Turbulent Shear Flows*, 141

Hamilton, D. Sommerville, J. H. and Stanford, P. N. 1980. Bottom currents and shelf sediments, southwest of Britain. *Sediment. Geol.*, **26**, 115

Hino, M. Kashiwayanag, M. Nakayama, A. and Hara, T. 1983. Experiments on the turbulence statistics and the structure of a reciprocating oscillatory flow. *J. Fluid Mech.*, **131**, 263

Jensen, B. L. Sumer, B. M. and Fredsøe, J. 1989. Turbulent oscillatory boundary layers at high Reynolds numbers. *J. Fluid Mech.*, **206**, 265

Jonssen, I. G. and Carlsen, N. A. 1976. Experimental and theoretical investigations in an oscillatory turbulent boundary layer. *J. Hydraul. Res.*, **14**, 45

Justesen, P. 1988. Prediction of turbulent oscillatory flow over rough beds. *Coastal Eng.*, **12**, 257

Justesen, P. and Fredsøe, J. 1985. Distribution of turbulence and suspended sediment in the wave boundary layer. *Tech. Rep. Prog. Rep. 62*, ISVA, Technical University of Denmark

Krishnappen, B. G. 1984. Laboratory verification of a turbulent flow model. *J. Hydraul. Eng. ASCE*, **110**, 500

Launder, B. E. Reece, G. J. and Rodi, W. 1975. Asymptotic near-wall stress dissipation rates in a turbulent flow. *J. Fluid Mech.*, **68**, 537

Launder, B. E. and Spalding, D. B. 1974. The numerical computation of turbulent flows. *Comput. Methods Appl. Mech. Eng.*, **3**, 269

Mendoza, C. and Shen, H. W. 1990. Investigation of turbulent flow over dunes. *J. Hydraul. Eng. ASCE*, **114**, 459

Nikuradse, J. 1933. Stromungsgesetze in rauhen Rohren. *Forschg. Geb. d. Ing.-Wesens*, Heft, 361

Sajjadi, S. G. and Aldridge, J. N. 1995. Prediction of turbulent flow over rough asymmetrical bed forms. *Appl. Math. Modelling*, **19**, 139

Schlichting, H. 1968. *Boundary-Layer Theory*, 6th ed. McGraw-Hill, New York

Shir, C. C. 1973. A preliminary study of atmospheric turbulent flow in the idealized planetary boundary layer. *J. Atmos. Sci.*, **30**, 1327

Sleath, J. F. A. 1987. Turbulent oscillatory flow over rough beds. *J. Mech. Eng.*, **182**, 369

Sleath, J. F. A. 1988. Transition in oscillatory flow over rough beds. *J. Wtrway., Port, Cstal., Ocean Eng.*, **114**, 18

Sumer, B. M. Jensen, B. L. and Fredsøe, J. 1988. Turbulence in oscillatory boundary layers. In *Advances in Turbulence*, G. Comte-Bellot and J. Mathieu (eds.), Springer-Verlag, Berlin, 556

Waywell, M. N. and Sajjadi, S. G. 1996. Transition from laminar to turbulence in oscillatory flows over a smooth flat plate. *Math. Eng. Ind.* (in press)